

See discussions, stats, and author profiles for this publication at: <https://www.researchgate.net/publication/263981689>

BiOCl/BiVO₄ p–n Heterojunction with Enhanced Photocatalytic Activity under Visible–Light Irradiation

ARTICLE *in* THE JOURNAL OF PHYSICAL CHEMISTRY C · DECEMBER 2013

Impact Factor: 4.77 · DOI: 10.1021/jp409598s

CITATIONS

63

READS

128

6 AUTHORS, INCLUDING:



Zhiqiao He

Zhejiang University of Technology

49 PUBLICATIONS 1,308 CITATIONS

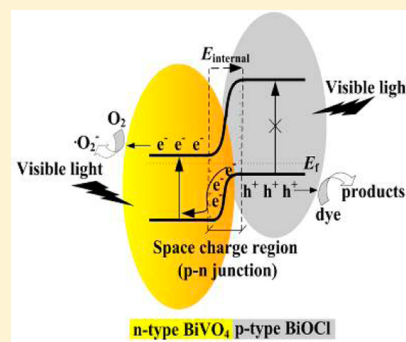
SEE PROFILE

BiOCl/BiVO₄ p–n Heterojunction with Enhanced Photocatalytic Activity under Visible-Light Irradiation

Zhiqiao He, Yuanqiao Shi, Chao Gao, Lina Wen, Jianmeng Chen, and Shuang Song*

College of Biological and Environmental Engineering, Zhejiang University of Technology, Hangzhou 310032, People's Republic of China

ABSTRACT: A novel visible-light-active BiOCl/BiVO₄ photocatalyst with a p–n heterojunction structure was prepared using a hydrothermal method. The photocatalytic activity of the heterojunction was investigated by monitoring the change in methyl orange (MO) concentration under visible-light irradiation. The results reveal that the composite exhibited markedly improved efficiency for MO photodegradation in comparison with pure BiVO₄, BiOCl, and Degussa P25. This is ascribed to the B-type heterojunction structure with a strong oxidative ability and efficient charge separation and transfer across the BiOCl/BiVO₄ p–n junction. The highest activity was obtained in the BiOCl/BiVO₄ heterojunction using a composite of 13 mol % BiOCl and 87 mol % BiVO₄. The removal of MO was mainly initiated by valence-band holes, but dissolved oxygen also played a crucial role in consuming the conduction-band electrons. This was verified by the effects of scavengers and N₂ purging.



1. INTRODUCTION

BiVO₄ exists in three main crystalline phases, monoclinic scheelite, with a band-gap energy of 2.4 eV, and the tetragonal zircon and tetragonal scheelite structures, both of which have a band-gap energy of 3.1 eV.^{1–3} Of these, monoclinic BiVO₄ has been of great interest for photochemical processes because of its narrow band gap and excellent photocatalytic performance under visible-light illumination.^{2–7} However, the low separation efficiency of photogenerated electrons and holes and poor electrical conductivity and adsorptive performance,^{8,9} limit wide application of BiVO₄ in the fields of environmental protection and solar conversion. As a result, many attempts have been made to overcome these disadvantages, including controlling the morphologies,^{7,10} forming composite structures or heterojunctions,¹¹ doping or composition tuning,¹² and coupling with oxygen-evolution catalysts.^{8,13}

Most recently, attention has been paid to the bismuth oxyhalides (BiOX, X = Cl, Br, I)¹⁴ and their composites in heterogeneous photocatalysis, owing to their characteristic hierarchical structures and unique optical properties.^{15,16} Among these bismuth oxyhalides, Bi-based oxychlorides have drawn considerable attention as novel photocatalysts because of their unique layered structures and high photocorrosion stability.¹⁷ The internal structure of [Bi₂O₂]²⁺ layers, interleaved by double slabs of Cl atoms,^{15,16,18} guides the growth of BiOCl along a particular axis to form a two-dimensional nanoplate morphology, favoring the transfer of electrons and holes generated inside the crystal surface and promoting electron/hole separation.¹⁹ However, BiOCl is a wide-band-gap ($E_g = 3.5$ eV) semiconductor^{20–22} and can only absorb ultraviolet light, which accounts for less than 5% of solar energy, leading to poor photocatalytic performance under visible-light irradiation.¹⁷

It is accepted that BiVO₄ and BiOCl are intrinsic n-type and p-type semiconductors, respectively.^{11,23,24} Theoretically, a p–n heterojunction will be formed when the two dissimilar crystalline semiconductors combine.²³ The heterojunction could provide a potential driving force, because of the building of an internal electric field, with its field direction from the n-type to the p-type semiconductor.^{9,23} As a result, the probability of recombination of photogenerated charge carriers is reduced.^{9,25}

In addition, the behavior of a semiconductor junction strongly depends on the alignment of the energy bands at the interface. Semiconductor interfaces can be organized into three types of heterojunctions: straddling gap, staggered gap, and broken gap.²⁶ In the staggered-gap type, the band gap of one material only partially overlaps with the band gap of the other material. Thus, in the case where the valence-band (VB) level of the visible-light-induced sensitizer (such as BiVO₄) is lower than that of the other UV-light-responsive semiconductor (such as BiOCl) in the heterojunction structure (denoted as a B-type heterojunction),²¹ the electrons in the VB of the UV-light-responsive semiconductor can be transferred to the VB of the sensitizer. As a consequence, the holes generated in the VB of the UV-light-responsive semiconductor could be involved in the oxidation reactions. Considering the strong oxidation ability of the photogenerated holes, the B-type heterojunction has received considerable attention as an alternative pathway for photocatalytic applications.²¹

However, to the best of our knowledge, the photocatalytic activity of BiOCl/BiVO₄ heterojunctions has not been reported. This novel system might have potential advantages,

Received: September 26, 2013

Revised: December 17, 2013

Published: December 17, 2013

such as the enhanced or tunable light absorption of BiVO_4 and BiOCl , an improvement of the photogenerated electron–hole separation, an enhancement of the interfacial charge transfer efficiency, and an improvement of the oxidation ability.

In this study, we successfully developed a series of highly active $\text{BiOCl}/\text{BiVO}_4$ heterojunction photocatalysts using a hydrothermal method. Techniques including X-ray diffraction (XRD), scanning electron microscopy (SEM), high-resolution transmission electron microscopy (HRTEM), the Brunauer–Emmett–Teller (BET) method, X-ray photoelectron spectroscopy (XPS), and UV–vis absorption spectroscopy were used to extensively characterize the photocatalytic materials. The photocatalytic efficiency of the prepared photocatalysts was correlated with the $\text{BiOCl}/\text{BiVO}_4$ molar ratio by studying the degradation of methyl orange (MO) dye under visible-light irradiation. The role of the main reactive species for the photocatalytic degradation of MO was elucidated through the use of different valence-band hole (h_{vb}^+), hydroxyl radical ($\cdot\text{OH}$), and conduction-band electron (e_{cb}^-) scavengers, as well as by N_2 purging.

2. EXPERIMENTAL METHODS

2.1. Reagents. All major chemicals were of analytical grade and were used as received, without further purification. The MO (molecular mass 327.3 g mol^{-1}) used in this study was produced by Shanghai SSS Reagent Co., Ltd. The NH_4VO_3 , $\text{Bi}(\text{NO}_3)_3 \cdot 5\text{H}_2\text{O}$, NaOH , and concentrated nitric acid (HNO_3 , 65 wt %), used to synthesize the BiVO_4 precursors, were purchased from Aladdin Reagent Co., Ltd., Shanghai, China. The concentrated hydrochloric acid (HCl , 36–38 wt %) for the preparation of BiOCl was obtained from Huadong Medicine Co., Ltd., Hangzhou, Zhejiang, China. The potassium iodide (KI), sodium fluoride (NaF), and *tert*-butanol (*t*-BuOH), used as scavengers, were purchased from Huadong Medicine Co., Ltd., Hangzhou, Zhejiang, China. Nitrogen (purity 99.99%) was supplied by Hangzhou Jingong Special Gas Co., Ltd., Hangzhou, China. All solutions were prepared with doubly distilled water.

2.2. Photocatalyst Synthesis. **2.2.1. Synthesis of BiVO_4 Powders.** The BiVO_4 photocatalyst was synthesized following a route similar to a previously published method.²⁷ Briefly, 0.04 mol of $\text{Bi}(\text{NO}_3)_3 \cdot 5\text{H}_2\text{O}$ in 40 mL of concentrated nitric acid and 0.04 mol NH_4VO_3 in 40 mL of 6 M NaOH were mixed together to form a suspension with a Bi/V molar ratio of 1:1. This was followed by 1 h of vigorous stirring in ambient air. Subsequently, an orange-yellow slurry-like mixture was obtained after the pH was adjusted to 11.0–12.0 by dropwise addition of diluted NaOH solution. The mixture was then transferred to a 200-mL Teflon-lined stainless steel autoclave and heated to 180°C ; this temperature was maintained for 6 h. Finally, the resulting precipitates were collected, washed with ethanol and deionized water, and dried at 60°C in air to obtain the BiVO_4 powders.

2.2.2. Synthesis of $\text{BiOCl}/\text{BiVO}_4$ Heterojunction Catalyst. The $\text{BiOCl}/\text{BiVO}_4$ heterojunction catalysts were synthesized using a simple method. Specifically, 0.5525 g of the BiVO_4 powder was added to 160 mL of HCl solution with different concentrations (3.20, 8.00, 42.67, 85.33 mM). After being stirred for 30 min, the resultant mixture was transferred to and sealed in a 200-mL Teflon-lined autoclave, heated to 180°C for 10 h, and cooled to room temperature naturally. The resulting $\text{BiOCl}/\text{BiVO}_4$ solids were thoroughly washed several times with ethanol and deionized water and dried at 80°C for 10 h.

The relative $\text{BiOCl}/\text{BiVO}_4$ mole ratio in the heterojunction catalyst was controlled by adjusting the concentration of HCl . The prepared samples are denoted as $x\text{BiOCl}/\text{BiVO}_4$, where x refers to the molar stoichiometric ratio calculated from the HCl/BiVO_4 ratio (initial Cl/Bi ratio).

2.3. Catalyst Characterization. Detailed crystallographic data for the prepared $\text{BiOCl}/\text{BiVO}_4$ samples were obtained using an X-ray diffractometer (Thermo ARL SCINTAG X'TRA diffractometer), using $\text{Cu K}\alpha$ radiation, operating at 45 kV and 40 mA.

Field-emission scanning electron microscopy (FE-SEM, Hitachi S-4800) was used to observe the morphology and surface properties of the photocatalysts.

Transmission electron microscopy (TEM) was performed with an FEI Tecnai G2 F30 microscope, operating at an accelerating voltage of 300 kV with 0.20-nm point resolution. This was used to characterize the structures of the catalysts.

The Brunauer–Emmett–Teller (BET) method was used to determine the total surface area of the prepared catalysts by physisorption of nitrogen, by means of a Micromeritics ASAP-2010 analyzer using liquid nitrogen at 77 K.

The surface-bonded states and the elemental composition of the photocatalysts were analyzed by X-ray photoelectron spectroscopy (XPS), with an RBD-upgraded PHI 5000 C ESCA system (Perkin-Elmer) using $\text{Mg K}\alpha$ radiation ($h\nu = 1253.6 \text{ eV}$).

The UV–vis absorption spectra of the catalysts were obtained using a UV–vis spectrophotometer (TU-1901, Pgeneral, China) in the range of 200–800 nm.

2.4. Photocatalytic Activity Measurements. The experimental apparatus for the photocatalytic reactions, shown in Figure 1, consisted of a cup-shaped pyrex glass

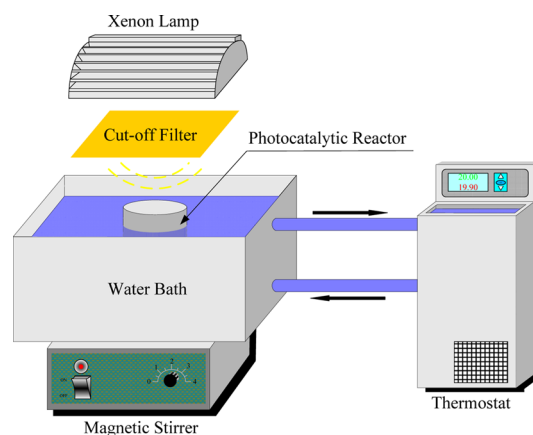


Figure 1. Apparatus for photocatalysis.

reactor (diameter, 50 mm; height, 70 mm; total capacity, 0.1 L) with a water bath, and a 500-W xenon lamp (Beijing Electric Light Sources Research Institute, Beijing, China) as the light source. A 400-nm cutoff filter (Shanghai Seagull Colored Optical Glass Co., Ltd., Shanghai, China) was employed to allow the desired irradiation intensity to be obtained. The distance between the light source and the top of the reaction solution was approximately 30 cm. The temperature of the bulk aqueous MO solution containing the catalysts was maintained at $20.0 \pm 1.0^\circ\text{C}$ by circulating cooling water from a thermostatted bath (THD-2015, Tianheng Instrument Factory, Ningbo, China).

The photocatalytic activity of the BiOCl/BiVO₄ heterojunction catalyst was evaluated by observing the decolorization of MO. In a typical operation, 0.1 g of catalyst was first dispersed in 0.1 L of deionized water. After ultrasonic irradiation for 30 min at room temperature, 2.63×10^{-6} mol of MO was added to the yellow catalyst suspension. The orange mixture obtained was then stirred for 30 min to ensure adsorption/desorption equilibrium between the MO and the photocatalyst powders. All experiments described above were undertaken in darkness. Subsequently, the mixed suspension was irradiated with visible light while being stirred magnetically. At regular intervals, 1 mL of suspension was sampled and filtered using a 0.45- μ m-pore-size membrane to remove photocatalyst particles.

In the photocatalytic studies in the presence of a radical scavenger, the scavengers were added at a 100-fold molar concentration relative to the initial MO concentration. In the dissolved-oxygen removal experiments, N₂ was prebubbled into the reaction solutions for approximately 30 min to obtain the desired oxygen level prior to visible-light irradiation.

The MO concentration was measured using a UV–vis spectrometer (T6, Beijing Purkinje General Instrument Co., Ltd.) set to the MO maximum absorption wavelength of 463 nm. The decoloration efficiency (DE) was calculated using the equation

$$DE = \frac{C_0 - C_t}{C_0} \times 100\% \quad (1)$$

where C_0 and C_t are the absorbances of the original solution and the photodegraded solution after time t , respectively.

2.5. Sample Analysis. To quantify the content of BiOCl in the synthesized composites, 0.1 g of the catalyst sample was completely dissolved in concentrated HNO₃. The solution was then injected into an ion chromatography setup (ICS-2000, Dionex, Sunnyvale, CA) to determine the concentration of chloride ions present in the solution. The ion chromatography setup was equipped with a dual-piston pump, a Dionex IonPac AS19 analytical column (4 × 250 mm), an IonPac AG19 guard column (4 × 250 mm), and a Dionex DS6 conductivity detector. Suppression of the eluent was achieved using a Dionex anion ASRS electrolytic suppressor (4 mm) in the autosuppression external water mode. The actual mole percentage of BiOCl in the heterojunction catalyst was then obtained, based on the mole percentage of chlorine, as shown in Table 1.

3. RESULTS AND DISCUSSION

3.1. Catalyst Characterization. **3.1.1. XRD Analysis.** The crystal structures of the BiOCl/BiVO₄ composite catalysts were identified by XRD analysis at room temperature. As the diffraction patterns in Figure 2 show, the diffraction peaks of the BiOCl/BiVO₄ composites are sharp, and the intensity of the diffraction peaks is high, indicating that the catalysts are well-crystallized. In addition, the diffraction peaks assigned to the monoclinic phase of BiVO₄ (JCPDS 14-0688) are accompanied by the characteristic peaks indexed to the tetragonal BiOCl (JCPDS 06-0249). No additional impurity phases were found in the diffraction patterns, suggesting that the BiOCl/BiVO₄ composites exhibit a coexistence of both BiVO₄ and BiOCl phases. Furthermore, with increasing content of BiOCl component in the BiOCl/BiVO₄ composites, the intensity of the (001) peak of the tetragonal-phase BiOCl

Table 1. Properties of Pure BiVO₄, Various BiOCl/BiVO₄ Heterojunctions, and Degussa P25

sample	actual composition ^a (mol %)		S_{BET} (m ² g ⁻¹)	DE (%)	DE/ S_{BET}
	IC	B–L			
BiVO ₄	0	0	0.950	24	25
0.3 BiOCl/BiVO ₄	13	11	2.512	67	27
0.75 BiOCl/BiVO ₄	14	13	2.802	85	30
4BiOCl/BiVO ₄	26	23	4.220	53	13
8 BiOCl/BiVO ₄	30	27	5.315	42	8
Degussa P25	–	–	56.000	45	0.8

^aIC and B–L denoted actual mole percentages of BiOCl in composites, as obtained by ion chromatography measurements and the Beer–Lambert law (according to UV–vis diffuse reflectance spectra), respectively.

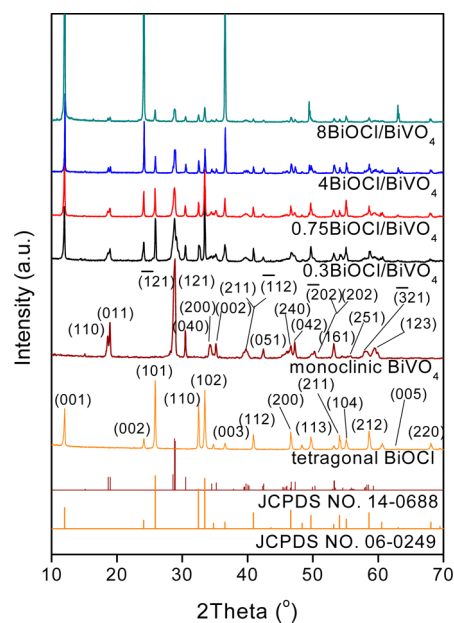


Figure 2. XRD patterns of monoclinic BiVO₄, tetragonal BiOCl, 0.3BiOCl/BiVO₄, 0.75BiOCl/BiVO₄, 4BiOCl/BiVO₄, and 8BiOCl/BiVO₄.

gradually increased, whereas the intensity of the ($\bar{1}21$) peak, intrinsic to the BiVO₄ phase, decreased. Note that the relative intensity of the diffraction peaks does not match well with the standard peaks, which might be due to the preferred orientation of the powder samples.

3.1.2. SEM and TEM Analysis. The morphology and crystal structure of 0.75BiOCl/BiVO₄ composites were obtained from SEM, TEM, and HRTEM images. The SEM image in Figure 3a indicates that the BiOCl/BiVO₄ composites were composed of microsheets, with an average width of 1–3 μ m and a thickness of 0.1–0.3 μ m, as well as dense particles with a diameter range of 0.3–0.7 μ m. The morphology and structure displayed in the TEM images agree well with that observed in the SEM image. In addition, an interface (highlighted by the white dotted line) between the sheet and the particle can be observed in the HRTEM image of the marked white rectangular section and is shown in the inset of Figure 3b. Observing both sides of the interface, the lattice fringes at 0.275 and 0.467 nm coincide with the fringe spacing of the (110) lattice plane of the tetragonal BiOCl sheet and the (011) crystal plane of the monoclinic

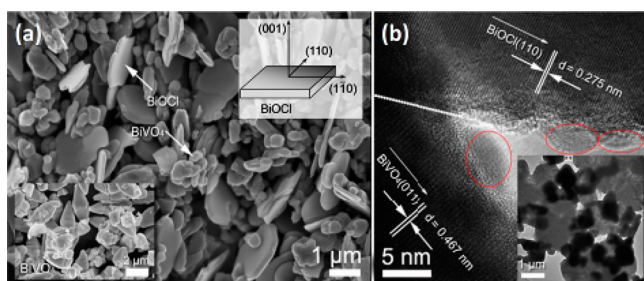


Figure 3. SEM, TEM, and HRTEM images of 0.75BiOCl/BiVO₄ composites: (a) SEM image of the BiOCl/BiVO₄ composite, where BiVO₄ particles and BiOCl sheets are marked with arrows, and (b) HRTEM image of the BiOCl/BiVO₄ composite, showing the lattice fringes (inset in b shows TEM image of BiOCl/BiVO₄ composites).

BiVO₄ particle, respectively.^{20,28} The obvious interface between the BiOCl sheet and the BiVO₄ particle implies the formation of a heterojunction structure.^{27,29,30} Moreover, according to the literature,²⁰ the bottom and top surfaces of the BiOCl sheet should be identified as {001} facets.

It is worth noting that some small granular particles (marked by the red ellipse in Figure 3b) emerged on the surface of individual BiVO₄ and BiOCl regions after beam exposure. This

might be because BiVO₄ and BiOCl are highly sensitive and melt when subjected to electron beam irradiation. A similar phenomenon has been observed elsewhere.^{7,31–33}

3.1.3. XPS Analysis. The chemical states of the 0.75BiOCl/BiVO₄ composite photocatalyst were investigated by XPS analysis, the results of which are shown in Figure 4. According to the XPS observations, only C, Bi, O, V, and Cl were detected in the sample. The C 1s peak at around 284.6 eV can be attributed to the signal from carbon contained in the instrument and was used for calibration.^{9,34–36} Two strong peaks in the high-resolution XPS spectra, at 164.4 and 159.0 eV, are assigned to Bi 4f_{5/2} and Bi 4f_{7/2}, respectively, which confirms that the bismuth species in the BiOCl/BiVO₄ composite is Bi³⁺ cations (Figure 4b).^{37,38} The characteristic spin–orbit splitting of V 2p_{1/2} and V 2p_{3/2} signals is observed at approximately 524.0 and 517.2 eV, respectively, corresponding to V⁵⁺ in BiVO₄ (Figure 4c).³⁴ In addition, the XPS signals for O 1s at a binding energy of 530.4 eV and Cl 2p at a binding energy of 198.0 eV correspond to the O^{2−} and Cl[−] anions, respectively, in BiOCl/BiVO₄ (Figure 4d,e).^{34,36} The results of the XPS analysis are consistent with those of the XRD analysis, further confirming the coexistence of BiVO₄ and BiOCl in the composite powders.

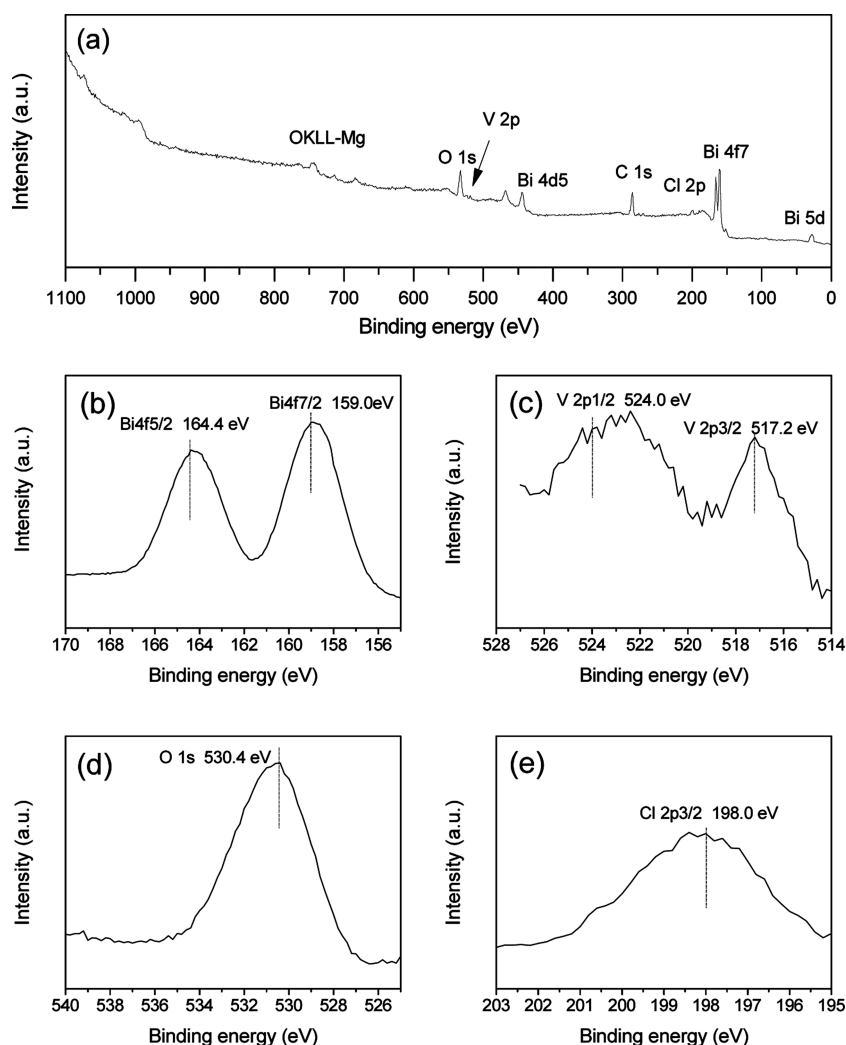


Figure 4. XPS patterns of the as-prepared 0.75BiOCl/BiVO₄ composite: (a) typical XPS survey, (b) Bi 4f, (c) V 2p, (d) O 1s, and (e) Cl 2p spectra.

3.1.4. BET Analysis. The BET surface areas (S_{BET}) of P25 and various prepared catalysts are listed in Table 1. The values of S_{BET} for P25 and pure BiVO_4 were 56.000 and $0.950 \text{ m}^2 \text{ g}^{-1}$, respectively. The composite samples generally had a larger BET surface area than the BiVO_4 bulk crystals, which is attributed to the conversion of granular BiVO_4 to BiOCl with sheet structures.³¹ Moreover, the S_{BET} value of the heterojunction catalysts increased gradually from 2.512 to $5.315 \text{ m}^2 \text{ g}^{-1}$ as the HCl/BiVO_4 molar ratio was increased from 0.3 to 8.

3.1.5. UV–Vis Diffuse Reflectance Spectroscopy. Figure 5 shows the UV–vis diffuse reflectance spectra of BiOCl , BiVO_4 ,

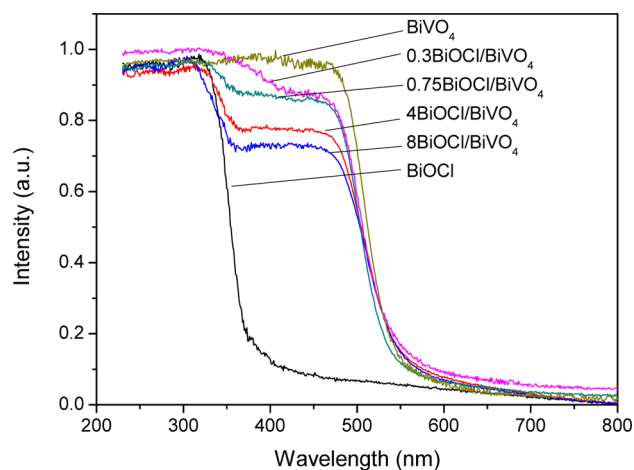


Figure 5. UV–vis diffuse reflectance spectra of pure BiVO_4 , $0.3\text{BiOCl}/\text{BiVO}_4$, $0.75\text{BiOCl}/\text{BiVO}_4$, $4\text{BiOCl}/\text{BiVO}_4$, $8\text{BiOCl}/\text{BiVO}_4$, and pure BiOCl .

and several $\text{BiOCl}/\text{BiVO}_4$ examples. The absorption edges of pure BiOCl and BiVO_4 occurred at about 360 and 520 nm, respectively. The band-gap energy was estimated to be 3.44 and 2.38 eV for BiOCl and BiVO_4 , respectively, and was calculated using the equation

$$\lambda_g = 1239.8/E_g \quad (2)$$

where λ_g is the band-gap wavelength and E_g is the band-gap energy.^{22,39} These results correspond well with those of previous reports.^{11,21,22,27} The $\text{BiOCl}/\text{BiVO}_4$ composites exhibited dual absorption edges at 360 and 520 nm, indicating the presence of BiOCl and BiVO_4 . Moreover, the absorbance in the 360–520-nm range gradually decreased with increasing BiOCl phase content in $\text{BiOCl}/\text{BiVO}_4$.

The relative concentrations of BiOCl and BiVO_4 in the heterojunction were determined from the Beer–Lambert law, as the absorbance is directly proportional to concentration. As listed in Table 1, the molar ratio of BiOCl to BiVO_4 obtained using this method was similar to that determined by the ion chromatography measurements.

3.2. Evaluation of the Photocatalytic Activity and Stability of the Catalysts. **3.2.1. Photoactivity.** The photocatalytic abilities of BiVO_4 , BiOCl , and the $\text{BiOCl}/\text{BiVO}_4$ composites were evaluated by observing the degradation of MO using commercial Degussa P25 as a control. The results are presented in Figure 6. Because of the chemical stability of MO, direct photolysis of the dye under visible irradiation ($\lambda > 400 \text{ nm}$) was negligible. In addition, after 11 h of visible irradiation, the DEs of MO over pure BiVO_4 and BiOCl were only 24% and 15%, respectively, indicating that the activity of

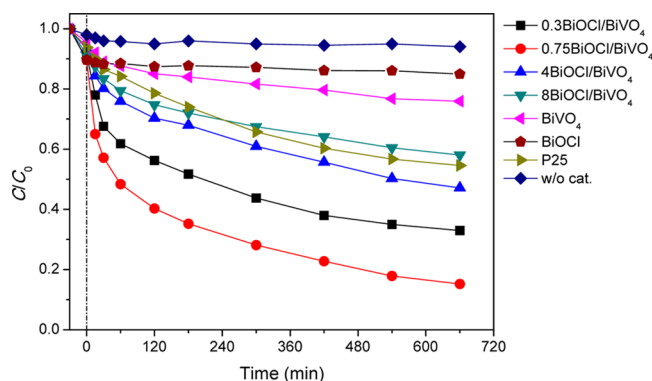


Figure 6. Plots of the MO concentration vs irradiation time, in the presence of various photocatalysts and in the absence of photocatalysts, under UV–vis irradiation. The initial concentration of MO was $2.63 \times 10^{-5} \text{ M}$, the catalyst dose was 1.0 g L^{-1} , and the reaction temperature was 20°C .

BiVO_4 with regard to MO degradation is poor and that any dye photosensitization by BiOCl can be neglected. In contrast, the $\text{BiOCl}/\text{BiVO}_4$ composites showed a sharp increase in MO degradation. As listed in Table 1, the MO degradation of the composite catalysts under visible irradiation decreased in the following order: $0.75\text{BiOCl}/\text{BiVO}_4 > 0.3\text{BiOCl}/\text{BiVO}_4 > 4\text{BiOCl}/\text{BiVO}_4 > 8\text{BiOCl}/\text{BiVO}_4$. In particular, the DE of $0.75\text{BiOCl}/\text{BiVO}_4$ exceeded those of P25 and BiVO_4 by factors of around 1.89 and 3.54, respectively.

It is well-known that an increase in specific surface area facilitates more effective adsorption on the photocatalyst surface, which might promote photocatalytic activity by increasing the concentration of reactants.⁴⁰ In other words, higher surface areas contribute to higher catalytic activities of heterojunction catalysts. To exclude the effect of surface area, the values of DE per unit surface area of the catalysts (DE/S_{BET}) were calculated, and the results are included in Table 1. After 11 h of reaction, the DE/S_{BET} value of $0.75\text{BiOCl}/\text{BiVO}_4$ was still 1.20 times higher than that of BiVO_4 . Accordingly, the dramatically enhanced degradation rate of MO cannot be justified by a simple improvement of the BET surface area.

It should be noted that the size of the synthesized BiVO_4 in this study was in the micrometer range (Figure 3a). Although nanostructured photocatalysts have the advantages of maximizing reactive surface area, they cannot completely support an internal space charge region, where the separation of photogenerated electrons and holes is greatly enhanced by the presence of an electric field.⁴¹ Furthermore, the probability of recombination of photogenerated electron–hole pairs on nanophotocatalysts and the back-reaction of intermediates are increased because the carriers and the reaction products are produced in close proximity and are thus not separated spatially.⁴² As a consequence, considering the electronic properties in particular, an ideal photocatalyst should absorb all light in an absorption length smaller than the width of the space charge region plus the carrier diffusion length, to ensure efficient separation of the photogenerated carriers.⁴¹

Generally, three main types of space charge regions for an n-type semiconductor (such as BiVO_4) can be distinguished: the accumulation layer, the depletion layer, and the inversion layer. The width of the space charge region in depletion (L_d) or accumulation (L_a) is related to the Debye length, L_D , and the potential drop across the space charge region, V_s .⁴³

$$L_D = (\epsilon_0 \epsilon_r kT / e^2 N_D)^{1/2} \quad (3)$$

where ϵ_0 represents the permittivity of free space, ϵ_r refers to the dielectric constant, k denotes the Boltzmann constant in eV K^{-1} , T is the absolute temperature, e is the electron charge, and N_D is the donor density for an n-type semiconductor. The widths of the space charge layers are given by

$$L_d = (2eV_s/kT)^{1/2} L_D \quad (4)$$

and

$$L_a = \sqrt{2} [1 - \exp(eV_s/2kT)] L_D \quad (5)$$

According to the literature,^{44,45} the values of N_D and ϵ_r are 10^{19} – 10^{20} cm^{-3} and 68, respectively, for $BiVO_4$. If we assume a reasonable value of 1 V for V_s , the width of the space charge region in $BiVO_4$ should be in the range 5–30 nm, because of the rather high values of N_D .

In addition, the carrier diffusion length can be obtained by

$$L = (D\tau)^{1/2} \quad (6)$$

with

$$D = kT\mu/e \quad (7)$$

where τ is the carrier lifetime and μ is the carrier mobility (4.4×10^{-2} $cm^2 V^{-1} s^{-1}$).⁴⁶

The lifetime of photogenerated carriers in $BiVO_4$ was estimated to be 40 ns.⁴⁶ From eqs 6 and 7, the carrier diffusion length was determined to be ~ 70 nm. Combining the above estimates, the optimum particle size for maximum absorption of light and separation of charge carriers was estimated to be in the range 150–200 nm. Moreover, using Beer's law, the light absorption length of $BiVO_4$ at the excitation wavelength of 400 nm was determined to be ~ 220 nm.^{41,47} Thus, for a 150–200-nm $BiVO_4$ particle, the excited charge carrier can diffuse to the space charge region where the charge carriers are easily separated by the local field and are less likely to recombine.⁴⁸ The size of the prepared $BiVO_4$ particles was in the range of 1–3 μm , as identified from the SEM images (inset in Figure 3a). Therefore, the bands in $BiVO_4$ can completely relax to the bulk level. In other words, the $BiVO_4$ particles are large enough to take advantage of band bending. However, the size of such pure-phase $BiVO_4$ is too large, resulting in a low surface area for efficient photocatalysis. As a result, efforts are still needed to optimize the particle size of $BiVO_4$ to provide a large enough density of reactive sites and effective separation of the photogenerated electron–hole pairs.

Because $BiOCl$ has negligible activity for MO degradation under visible-light irradiation, the improved photocatalytic activity after addition of $BiOCl$ to the photocatalytic materials must be due to the formation of the heterojunction structure. Monoclinic $BiVO_4$ is normally an intrinsic n-type semiconductor, whereas $BiOCl$ exhibits the characteristic properties of a p-type semiconductor. When $BiVO_4$ and $BiOCl$ form a heterojunction after being closely joined together, an internal static electric field (E_{internal}) is formed at the interface between them, with the electric field direction from $BiVO_4$ to $BiOCl$, so that the Fermi levels (E_f) equilibrate. As a consequence of the formation of a space charge region at the interface of the semiconductors after electron transfer, the $BiVO_4$ and $BiOCl$ bands will bend. The mean lifetime of a single electron–hole pair is on the nanosecond scale in a semiconductor particle,⁴⁹ whereas charge transfer across the interface between semi-

conductors can be completed within picoseconds.⁴¹ Therefore, heterostructured photocatalysts offer extra opportunities to depress both the bulk and surface recombination of photo-generated carriers.⁵⁰

Moreover, the band-edge positions of the conduction band (CB) and VB of $BiVO_4$ are approximately 0.33 and 2.75 eV, respectively, whereas those of $BiOCl$ are at approximately –1.10 and 2.40 eV, respectively.^{11,20,21} Therefore, in the $BiOCl/BiVO_4$ heterojunction, the CB of $BiVO_4$ is positioned between the VB and CB of $BiOCl$, and the VB of $BiVO_4$ is 0.35 eV lower than that of $BiOCl$. Unlike an A-type heterojunction, where holes are not generated on the nonexcited semiconductor in the heterojunction structure under visible-light irradiation, the $BiOCl/BiVO_4$ composite therefore belongs to the “B-type heterojunction” class.^{21,39} The relative band energy positions between $BiVO_4$ and $BiOCl$ enhance the efficient photocatalytic degradation of MO. Figure 7 shows schemati-

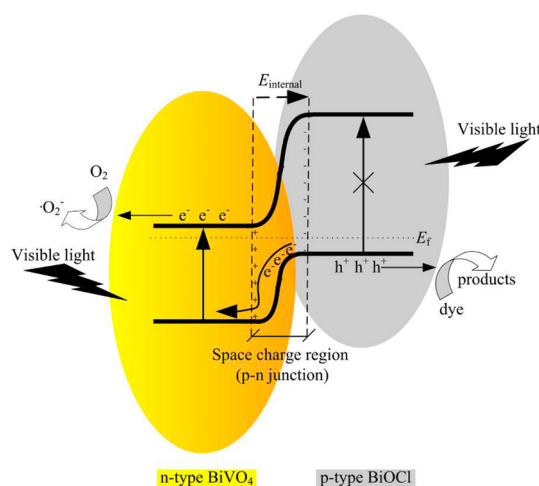


Figure 7. Highly simplified schematic diagram of the formation of a p–n junction and the possible charge-separation process.

cally the B-type heterojunction structure formed by $BiVO_4$ and $BiOCl$. In the presence of visible-light radiation, $BiVO_4$ behaves as a sensitizer, because it is easily excited by visible radiation, resulting in the VB of $BiVO_4$ becoming partially vacant. In contrast, $BiOCl$, with an E_g value of 3.5 eV, cannot be excited in this case. Because the electric field at the interface facilitates the migration of electrons from the VB of the p-type semiconductor to the VB of the n-type semiconductor,^{25,51–53} the electrons in the VB of $BiOCl$ could easily be transferred to the VB of $BiVO_4$ as holes are generated in the VB of $BiOCl$. The holes in the VB of $BiOCl$ could initiate photocatalytic oxidation reactions, and the excited electrons in the CB of $BiVO_4$ create a simultaneous reduction reaction. In other words, the internal field created by the B-type heterojunction between $BiVO_4$ and $BiOCl$ promotes the separation of photogenerated charge carriers and the spatially selective oxidation and reduction.

From the above discussion, it can be deduced that the fabrication of enough interfaces with high quality in the heterostructured catalysts plays a key role in improving the photocatalytic performance. In this study, the optimal initial Cl/Bi ratio for MO degradation was found to be 0.75. It is straightforward to assume that the optimum photocatalytic activity is directly related to an increase in charge separation due to the formation of the maximum number of space charge

regions (or E_{internal}) on BiVO_4 by the addition of BiOCl . However, this conclusion requires further confirmation.

3.2.2. Photostability. The stability of the heterojunction photocatalyst was evaluated by repeating experiments on the degradation of MO under visible irradiation, using $0.75\text{BiOCl}/\text{BiVO}_4$. After each run, the catalysts were collected and washed by simple filtration followed by ultrasonic cleaning with deionized water. As shown in Figure 8, the photocatalytic

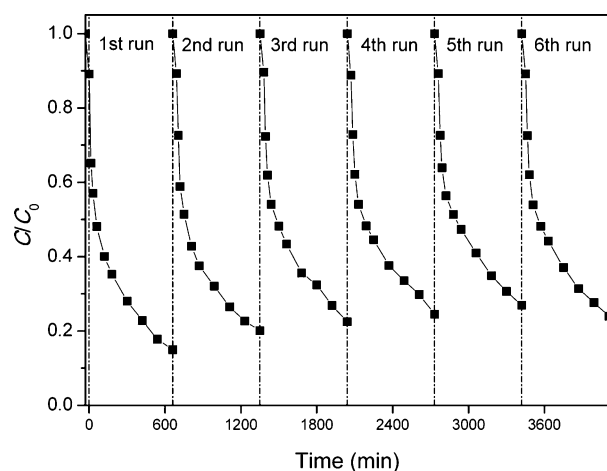
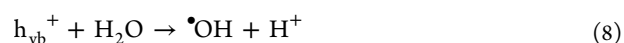


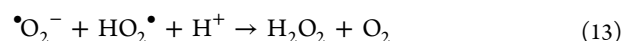
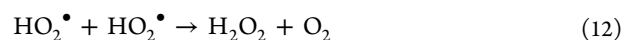
Figure 8. Cyclic degradation curve for the $0.75\text{BiOCl}/\text{BiVO}_4$ photocatalyst.

efficiency did not show significant loss after five successive cycles, indicating that the heterojunction photocatalysts were relatively effective and stable and were not photocorroded during the photocatalytic degradation of MO under visible irradiation.

3.3. Discussion of the Effects of Reactive Species on the Photodegradation of MO. It is generally accepted that the photocatalytic process is induced by photochemically generated electron–hole pairs. Subsequently, in addition to the active hole and electron processes, the holes can react with preadsorbed $\text{H}_2\text{O}/\text{OH}^-$ on the catalyst surface to yield $\cdot\text{OH}$.^{54–57}



and dissolved oxygen in the solution can trap electrons to produce the reactive superoxide radical ($\cdot\text{O}_2^-$), which spontaneously transforms into $\text{HO}_2\cdot$ and H_2O_2 .^{54–57}



To estimate the influence of these reactive species on the photocatalytic reactions, radical scavengers (fluoride ion, iodide ion, and $t\text{-BuOH}$), in addition to N_2 purging, were applied to the process of MO degradation using the $0.75\text{BiOCl}/\text{BiVO}_4$ heterojunction catalyst.

3.3.1. Effects of Fluoride Ions, Iodide Ion, and $t\text{-BuOH}$. Because the redox potential of the $\text{F}^\bullet/\text{F}^-$ couple is around 3.6 V, fluoride can be strongly adsorbed on the surface of catalysts

to form chemical bonds, and the adsorbed fluoride is very stable against oxidation, even by h_{vb}^+ .^{57,58} Based on this fact, the addition of excess NaF to the reaction solution could significantly prevent MO from being adsorbed onto the surface of the catalysts. Comparison of curves 1 and 4 in Figure 9

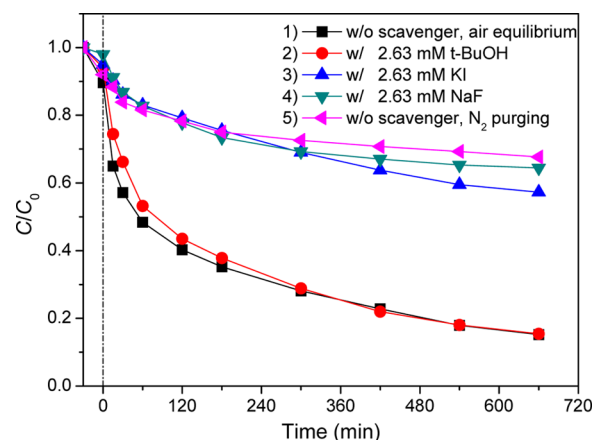
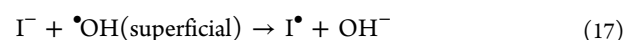


Figure 9. Change in concentration of MO in the presence of the $0.75\text{BiOCl}/\text{BiVO}_4$ photocatalyst under visible irradiation: in the presence of scavengers in an air equilibrium system, without scavengers in an air equilibrium system, and without scavengers in a N_2 -purged system.

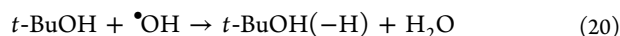
indicates that decolorization of MO was strongly inhibited by the addition of a 100-fold molar concentration (with respect to the initial MO concentration) of NaF. This result suggests that MO was mainly decolorized by a surface charge process. In other words, MO is preferentially adsorbed onto the active sites of catalysts before reacting with the active species.

The redox potential of the $\text{I}^\bullet/\text{I}^-$ pair is 1.3 V.⁵⁷ Thus, the iodide ion can act as an excellent scavenger, quenching h_{vb}^+ and superficial $\cdot\text{OH}$ generated in the photocatalytic reaction,^{57,59} by the following reaction pathway^{60,61}



As a result, the amount of oxidizing species on the surface of the catalyst available for reaction with MO is reduced. As shown in Figure 9, when 2.63 mM KI was used to quench h_{vb}^+ and superficial $\cdot\text{OH}$ was generated, the MO decolorization was significantly inhibited. Accordingly, the photocatalytic process must be initiated by the h_{vb}^+ and/or superficial $\cdot\text{OH}$ pathways. It should be noted that the absorption peak of KI is at 220 nm, and the I_2 aqueous solution has two prominent absorption peaks, at 287 and 353 nm.^{57,62} Hence, the quantitative determination of MO at the characteristic wavelength of 463 nm, obtained by UV–vis spectrophotometry, was not influenced by the addition of KI.

$t\text{-BuOH}$ is a well-known $\cdot\text{OH}$ scavenger, which can react quickly with $\cdot\text{OH}$ with a rate constant of $6.0 \times 10^8 \text{ M}^{-1} \text{ s}^{-1}$.^{60,63}



Excess *t*-BuOH, with a 100-fold molar concentration relative to the concentration of MO, was added as an $\bullet\text{OH}$ radical scavenger to examine the effect of $\bullet\text{OH}$ radical on the photocatalytic degradation of MO. The results are shown in Figure 9. The decolorization of MO was determined to be almost unchanged in the presence and absence of *t*-BuOH, implying that the $\bullet\text{OH}$ radical does not play a major role in MO decolorization.

Combining the experimental results from the additions of excess NaF, KI, and *t*-BuOH, it can be concluded that $h\nu_{\text{vb}}^+$ on the photocatalyst surface is the predominant contributor to the degradation of MO.

3.3.2. Effects of the N_2 Purging Experiment. Molecular oxygen generally acts as an electron acceptor, preventing undesired electron–hole recombination through the formation of dioxide radicals ($\text{O}_2^{\bullet-}$ and HO_2^{\bullet}) in the heterogeneous system.^{57,64} To investigate the effect of dissolved oxygen, a N_2 purging experiment was conducted and compared with the results obtained under air-equilibrated conditions. In our experiments, when the level of dissolved oxygen was controlled to be below 0.15 mM in water,^{60,62,64} the photocatalytic decolorization efficiency of MO showed an obvious decrease in comparison with the case of the air-equilibrated solution. This experimental observation demonstrates that dissolved oxygen plays an important role in heterogeneous photocatalysis, so the e_{cb}^- pathway cannot be ignored. Further work is needed to determine the role of oxygen during the photocatalysis by using an oxygen isotope tracing method.^{65–67}

Combining the above effects, a possible pathway for the degradation of MO by the BiOCl/BiVO₄ heterojunction photocatalyst is depicted in Figure 7. The BiVO₄ in the BiOCl/BiVO₄ system acts as a sensitizer for visible radiation response. Under visible irradiation, the absorption of photons by BiVO₄ leads to excitation of the electrons from its VB to its CB, leaving holes in the VB. Then, the electrons in the VB of BiOCl transfer to the VB of BiVO₄. Because the B-type heterojunction structure is formed by partially converting BiVO₄ into BiOCl, the internal electrostatic potential (with electric field direction from BiVO₄ to BiOCl) at the p–n junction between BiOCl and BiVO₄ promotes the electron migration process. Finally, the excited electrons in the CB of BiVO₄ react with dissolved oxygen to generate a series of reactive species, whereas the holes accumulated in the VB of BiOCl react with MO adsorbed on the catalyst surface to generate degradation products.

4. CONCLUSIONS

A series of BiOCl/BiVO₄ heterojunction photocatalysts have been successfully synthesized by a hydrothermal method. The molar ratio of BiVO₄ to BiOCl has a significant influence on the activity of the photocatalysts. When the system was irradiated with visible light for 11 h, the efficiency of the decomposition of MO with the most active 0.75BiOCl/BiVO₄ heterojunction was 85%, which is approximately 3.54 and 1.89 times greater than the decompositions obtained with pure BiVO₄ and commercially available Degussa P25, respectively. Moreover, the efficient visible radiation-activated BiOCl/BiVO₄ photocatalyst remained stable after five irradiation cycles. Enhancement of the decomposition of MO using BiOCl/BiVO₄ photocatalysts is attributed to the formation of B-type p–n heterojunctions between BiOCl and BiVO₄, leading to an effective separation of

photogenerated electrons and holes. Based on free-radical scavenging and N_2 -purging experiments, the photogenerated holes in the valence bands of BiOCl were demonstrated to be responsible for the direct oxidation of MO. The role of the photogenerated electrons in the conduction bands of BiVO₄ is to react with dissolved oxygen. Ultimately, with further improvement and optimization, the BiOCl/BiVO₄ heterojunction photocatalysts might be a viable alternative for photocatalytic applications.

AUTHOR INFORMATION

Corresponding Author

*Tel.: 86-571-88320726. Fax: 86-571-88320726. E-mail: ss@zjut.edu.cn.

Notes

The authors declare no competing financial interest.

ACKNOWLEDGMENTS

This work was supported by the Program for Changjiang Scholars and Innovative Research Team in University (Grant IRT13096), the National Natural Science Foundation of China (Grants 21076196 and 21177115) and the Zhejiang Provincial Natural Science Foundation of China (Grant LR13B070002).

REFERENCES

- (1) Chaiwichian, S.; Inceesungvorn, B.; Pingmuang, K.; Wetchakun, K.; Phanichphant, S.; Wetchakun, N. Synthesis and Characterization of the Novel BiVO₄/CeO₂ Nanocomposites. *Eng. J.* **2012**, *16*, 153–160.
- (2) Martínez-de la Cruz, A.; García-Pérez, U. M.; Sepúlveda-Guzmán, S. Characterization of the Visible-Light-Driven BiVO₄ Photocatalyst Synthesized via a Polymer-Assisted Hydrothermal Method. *Res. Chem. Intermed.* **2012**, *39*, 881–894.
- (3) Tokunaga, S.; Kato, H.; Kudo, A. Selective Preparation of Monoclinic and Tetragonal BiVO₄ with Scheelite Structure and Their Photocatalytic Properties. *Chem. Mater.* **2001**, *13*, 4624–4628.
- (4) Zhang, J. Y.; Luo, W. J.; Li, W.; Zhao, X.; Xue, G. G.; Yu, T.; Zhang, C. F.; Xiao, M.; Li, Z. S.; Zou, Z. G. A Dye-Free Photoelectrochemical Solar Cell Based on BiVO₄ with a Long Lifetime of Photogenerated Carriers. *Electrochem. Commun.* **2012**, *22*, 49–52.
- (5) Kudo, A.; Omori, K.; Kato, H. A Novel Aqueous Process for Preparation of Crystal Form-Controlled and Highly Crystalline BiVO₄ Powder from Layered Vanadates at Room Temperature and Its Photocatalytic and Photophysical Properties. *J. Am. Chem. Soc.* **1999**, *121*, 11459–11467.
- (6) Kudo, A.; Ueda, K.; Kato, H.; Mikami, I. Photocatalytic O₂ Evolution under Visible Light Irradiation on BiVO₄ in Aqueous AgNO₃ Solution. *Catal. Lett.* **1998**, *53*, 229–230.
- (7) Zhang, L.; Chen, D. R.; Jiao, X. L. Monoclinic Structured BiVO₄ Nanosheets: Hydrothermal Preparation, Formation Mechanism, and Coloristic and Photocatalytic Properties. *J. Phys. Chem. B* **2006**, *110*, 2668–2673.
- (8) Park, Y.; McDonald, K. J.; Choi, K.-S. Progress in Bismuth Vanadate Photoanodes for Use in Solar Water Oxidation. *Chem. Soc. Rev.* **2013**, *42*, 2321.
- (9) Long, M. C.; Cai, W. M.; Cai, J.; Zhou, B. X.; Chai, X. Y.; Wu, Y. H. Efficient Photocatalytic Degradation of Phenol over Co₃O₄/BiVO₄ Composite under Visible Light Irradiation. *J. Phys. Chem. B* **2006**, *110*, 20211–20216.
- (10) Yu, J. Q.; Kudo, A. Effects of Structural Variation on the Photocatalytic Performance of Hydrothermally Synthesized BiVO₄. *Adv. Funct. Mater.* **2006**, *16*, 2163–2169.
- (11) Chen, L.; Zhang, Q.; Huang, R.; Yin, S.-F.; Luo, S.-L.; Au, C.-T. Porous Peanut-Like Bi₂O₃–BiVO₄ Composites with Heterojunctions: One-Step Synthesis and Their Photocatalytic Properties. *Dalton Trans.* **2012**, *41*, 9513.

- (12) Pilli, S. K.; Furtak, T. E.; Brown, L. D.; Deutsch, T. G.; Turner, J. A.; Herring, A. M. Cobalt-Phosphate (Co-Pi) Catalyst Modified Mo-Doped BiVO₄ Photoelectrodes for Solar Water Oxidation. *Energy Environ. Sci.* **2011**, *4*, 5028.
- (13) Pilli, S. K.; Deutsch, T. G.; Furtak, T. E.; Turner, J. A.; Brown, L. D.; Herring, A. M. Light Induced Water Oxidation on Cobalt-Phosphate (Co-Pi) Catalyst Modified Semi-Transparent, Porous SiO₂-BiVO₄ Electrodes. *Phys. Chem. Chem. Phys.* **2012**, *14*, 7032–7039.
- (14) Wang, C. H.; Shao, C. L.; Liu, Y. C.; Zhang, L. N. Photocatalytic Properties BiOCl and Bi₂O₃ Nanofibers Prepared by Electrospinning. *Scripta Mater.* **2008**, *59*, 332–335.
- (15) Zhao, L. J.; Zhang, X. C.; Fan, C. M.; Liang, Z. H.; Han, P. D. First-Principles Study on the Structural, Electronic and Optical Properties of BiOX (X = Cl, Br, I) Crystals. *Physica B* **2012**, *407*, 3364–3370.
- (16) Zhang, X.; Ai, Z. H.; Jia, F. L.; Zhang, L. Z. Generalized One-Pot Synthesis, Characterization, and Photocatalytic Activity of Hierarchical BiOX (X = Cl, Br, I) Nanoplate Microspheres. *J. Phys. Chem. C* **2008**, *112*, 747–753.
- (17) Shenawi-Khalil, S.; Uvarov, V.; Menes, E.; Popov, I.; Sasson, Y. New Efficient Visible Light Photocatalyst Based on Heterojunction of BiOCl–Bismuth Oxide. *Appl. Catal. A* **2012**, *413*–*414*, 1–9.
- (18) Ye, L. Q.; Zan, L.; Tian, L. H.; Peng, T. Y.; Zhang, J. J. The {001} Facets-Dependent High Photoactivity of BiOCl Nanosheets. *Chem. Commun.* **2011**, *47*, 6951–6953.
- (19) Dong, F.; Sun, Y. J.; Fu, M.; Wu, Z. B.; Lee, S. C. Room Temperature Synthesis and Highly Enhanced Visible Light Photocatalytic Activity of Porous BiOI/BiOCl Composites Nanoplates Microflow. *J. Hazard. Mater.* **2012**, *219*–*220*, 26–34.
- (20) Jiang, J.; Zhao, K.; Xiao, X. Y.; Zhang, L. Z. Synthesis and Facet-Dependent Photoreactivity of BiOCl Single-Crystalline Nanosheets. *J. Am. Chem. Soc.* **2012**, *134*, 4473–4476.
- (21) Chai, S. Y.; Kim, Y. J.; Jung, M. H.; Chakraborty, A. K.; Jung, D.; Lee, W. I. Heterojunctioned BiOCl/Bi₂O₃, a New Visible Light Photocatalyst. *J. Catal.* **2009**, *262*, 144–149.
- (22) Zhang, K. L.; Liu, C. M.; Huang, F. Q.; Zheng, C.; Wang, W. D. Study of the Electronic Structure and Photocatalytic Activity of the BiOCl Photocatalyst. *Appl. Catal. B* **2006**, *68*, 125–129.
- (23) Guan, M.-L.; Ma, D.-K.; Hu, S.-W.; Chen, Y.-J.; Huang, S.-M. From Hollow Olive-Shaped BiVO₄ to n-p Core-Shell BiVO₄@Bi₂O₃ Microspheres: Controlled Synthesis and Enhanced Visible-Light-Responsive Photocatalytic Properties. *Inorg. Chem.* **2011**, *50*, 800–805.
- (24) Michel, C. R.; Contreras, N. L. L.; Martínez-Preciado, A. H. Gas Sensing Properties of Nanostructured Bismuth Oxide. *Sens. Actuators B* **2011**, *160*, 271–277.
- (25) Yu, H. B.; Chen, S.; Quan, X.; Zhao, H. M.; Zhang, Y. B. Fabrication of a TiO₂-BDD Heterojunction and Its Application as a Photocatalyst for the Simultaneous Oxidation of an Azo Dye and Reduction of Cr(VI). *Environ. Sci. Technol.* **2008**, *42*, 3791–3796.
- (26) Yan, D. H.; Wang, H. B.; Du, B. X. *Introduction to Organic Semiconductor Heterojunctions*; Science Press: Beijing, China, 2008.
- (27) Hu, Y.; Li, D. Z.; Zheng, Y.; Chen, W.; He, Y. H.; Shao, Y.; Fu, X. Z.; Xiao, G. C. BiVO₄/TiO₂ Nanocrystalline Heterostructure: A Wide Spectrum Responsive Photocatalyst towards the Highly Efficient Decomposition of Gaseous Benzene. *Appl. Catal. B* **2011**, *104*, 30–36.
- (28) Ren, L.; Ma, L. L.; Jin, L.; Wang, J.-B.; Qiu, M. Q.; Yu, Y. Template-Free Synthesis of BiVO₄ Nanostructures: II. Relationship between Various Microstructures for Monoclinic BiVO₄ and Their Photocatalytic Activity for the Degradation of Rhodamine B under Visible Light. *Nanotechnology* **2009**, *20*, 405602.
- (29) Zhu, G. X.; Xu, Z. Controllable Growth of Semiconductor Heterostructures Mediated by Bifunctional Ag₂S Nanocrystals as Catalyst or Source-Host. *J. Am. Chem. Soc.* **2011**, *133*, 148–157.
- (30) Wang, C.; Tian, W. D.; Ding, Y.; Ma, Y. Q.; Wang, Z. L.; Markovic, N. M.; Stamenkovic, V. R.; Daimon, H.; Sun, S. H. Rational Synthesis of Heterostructured Nanoparticles with Morphology Control. *J. Am. Chem. Soc.* **2010**, *132*, 6524–6529.
- (31) Madhusudan, P.; Ran, J. R.; Zhang, J.; Yu, J. G.; Liu, G. Novel Urea Assisted Hydrothermal Synthesis of Hierarchical BiVO₄/Bi₂O₃CO₃ Nanocomposites with Enhanced Visible-Light Photocatalytic Activity. *Appl. Catal. B* **2011**, *110*, 286–295.
- (32) Zhang, Z. B.; Gekhtman, D.; Dresselhaus, M. S.; Ying, J. Y. Processing and Characterization of Single-Crystalline Ultrafine Bismuth Nanowires. *Chem. Mater.* **1999**, *11*, 1659–1665.
- (33) Li, Y. D.; Wang, J. W.; Deng, Z. X.; Wu, Y. Y.; Sun, X. M.; Yu, D. P.; Yang, P. D. Bismuth Nanotubes: A Rational Low-Temperature Synthetic Route. *J. Am. Chem. Soc.* **2001**, *123*, 9904–9905.
- (34) Su, J.; Zou, X.-X.; Li, G.-D.; Wei, X.; Yan, C.; Wang, Y.-N.; Zhao, J.; Zhou, L.-J.; Chen, J.-S. Macroporous V₂O₅-BiVO₄ Composites: Effect of Heterojunction on the Behavior of Photo-generated Charges. *J. Phys. Chem. C* **2011**, *115*, 8064–8071.
- (35) Wang, H. Q.; Wu, Z. B.; Liu, Y. A Simple Two-Step Template Approach for Preparing Carbon-Doped Mesoporous TiO₂ Hollow Microspheres. *J. Phys. Chem. C* **2009**, *113*, 13317–13324.
- (36) Zhang, J.; Xia, J. X.; Yin, S.; Li, H. M.; Xu, H.; He, M. Q.; Huang, L. Y.; Zhang, Q. Improvement of Visible Light Photocatalytic Activity over Flower-Like BiOCl/BiOBr Microspheres Synthesized by Reactable Ionic Liquids. *Colloids Surf. A* **2013**, *420*, 89–95.
- (37) Zhou, B.; Qu, J. H.; Zhao, X.; Liu, H. J. Fabrication and Photoelectrocatalytic Properties of Nanocrystalline Monoclinic BiVO₄ Thin-Film Electrode. *J. Environ. Sci.* **2011**, *23*, 151–159.
- (38) Wang, M.; Liu, Q.; Che, Y. S.; Zhang, L. F.; Zhang, D. Characterization and Photocatalytic Properties of N-Doped BiVO₄ Synthesized via a Sol-Gel Method. *J. Alloys Compd.* **2013**, *548*, 70–76.
- (39) Shamaila, S.; Sajjad, A. K. L.; Chen, F.; Zhang, J. L. WO₃/BiOCl, a Novel Heterojunction as Visible Light Photocatalyst. *J. Colloid Interface Sci.* **2011**, *356*, 465–472.
- (40) Qi, K. H.; Chen, X. Q.; Liu, Y. Y.; Xin, J. H.; Mak, C. L.; Daoud, W. A. Facile Preparation of Anatase/SiO₂ Spherical Nanocomposites and Their Application in Self-Cleaning Textiles. *J. Mater. Chem.* **2007**, *17*, 3504–3508.
- (41) Li, L.; Salvador, P. A.; Rohrer, G. S. Photocatalysts with Internal Electric Fields. *Nanoscale* **2014**, *6*, 24–42.
- (42) Li, L.; Liu, X.; Zhang, Y. L.; Salvador, P. A.; Rohrer, G. S. Heterostructured (Ba,Sr)TiO₃/TiO₂ Core/Shell Photocatalysts: Influence of Processing and Structure on Hydrogen Production. *Int. J. Hydrogen Energy* **2013**, *38*, 6948–6959.
- (43) Mönch, W. *Electronic Properties of Semiconductor Interfaces*; Springer-Verlag: New York, 2004.
- (44) Abdi, F. F. Towards Highly Efficient Bias-Free Solar Water Splitting. Ph.D. Thesis, Delft University of Technology, Delft, The Netherlands, 2013.
- (45) Valant, M.; Suvorov, D. Chemical Compatibility between Silver Electrodes and Low-Firing Binary-Oxide Compounds: Conceptual Study. *J. Am. Ceram. Soc.* **2000**, *83*, 2721–2729.
- (46) Abdi, F. F.; Savenije, T. J.; May, M. M.; Dam, B.; van de Krol, R. The Origin of Slow Carrier Transport in BiVO₄ Thin Film Photoanodes: A Time-Resolved Microwave Conductivity Study. *J. Phys. Chem. Lett.* **2013**, *4*, 2752–2757.
- (47) Zhao, Z. Y.; Li, Z. S.; Zou, Z. G. Electronic Structure and Optical Properties of Monoclinic Clinobisvanite BiVO₄. *Phys. Chem. Chem. Phys.* **2011**, *13*, 4746–4753.
- (48) Nozik, A. J.; Memming, R. Physical Chemistry of Semiconductor-Liquid Interfaces. *J. Phys. Chem.* **1996**, *100*, 13061–13078.
- (49) Linsebigler, A. L.; Lu, G. Q.; Yates, J. T. Photocatalysis on TiO₂ Surfaces: Principles, Mechanisms, and Selected Results. *Chem. Rev.* **1995**, *95*, 735–758.
- (50) Yang, G. R.; Zhang, Q.; Chang, W.; Yan, W. Fabrication of Cd_{1-x}Zn_xS/TiO₂ Heterostructures with Enhanced Photocatalytic Activity. *J. Alloys Compd.* **2013**, *580*, 29–36.
- (51) Chen, Y. S.; Crittenden, J. C.; Hackney, S.; Sutter, L.; Hand, D. W. Preparation of a Novel TiO₂-Based p-n Junction Nanotube Photocatalyst. *Environ. Sci. Technol.* **2005**, *39*, 1201–1208.
- (52) Dai, G. P.; Yu, J. G.; Liu, G. Synthesis and Enhanced Visible-Light Photoelectrocatalytic Activity of p-n Junction BiOI/TiO₂ Nanotube Arrays. *J. Phys. Chem. C* **2011**, *115*, 7339–7346.

- (53) Chai, S. N.; Zhao, G. H.; Zhang, Y.-n.; Wang, Y. J.; Nong, F. Q.; Li, M. F.; Li, D. M. Selective Photoelectrocatalytic Degradation of Recalcitrant Contaminant Driven by an n-P Heterojunction Nanoelectrode with Molecular Recognition Ability. *Environ. Sci. Technol.* **2012**, *46*, 10182–10190.
- (54) Tseng, D.-H.; Juang, L.-C.; Huang, H.-H. Effect of Oxygen and Hydrogen Peroxide on the Photocatalytic Degradation of Monochlorobenzene in TiO₂ Aqueous Suspension. *Int. J. Photoenergy* **2012**, *2012*, 1–9.
- (55) Zhang, D. D.; Qiu, R. L.; Song, L.; Eric, B.; Mo, Y. Q.; Huang, X. F. Role of Oxygen Active Species in the Photocatalytic Degradation of Phenol Using Polymer Sensitized TiO₂ under Visible Light Irradiation. *J. Hazard. Mater.* **2009**, *163*, 843–847.
- (56) Konstantinou, I. K.; Albanis, T. A. TiO₂-Assisted Photocatalytic Degradation of Azo Dyes in Aqueous Solution: Kinetic and Mechanistic Investigations: A Review. *Appl. Catal. B* **2004**, *49*, 1–14.
- (57) Song, S.; Xu, L. J.; He, Z. Q.; Chen, J. M.; Xiao, X. Z.; Yan, B. Mechanism of the Photocatalytic Degradation of C.I. Reactive Black 5 at pH 12.0 Using SrTiO₃/CeO₂ as the Catalyst. *Environ. Sci. Technol.* **2007**, *41*, 5846–5853.
- (58) Yang, S. Y.; Lou, L. P.; Wang, K.; Chen, Y. X. Shift of Initial Mechanism in TiO₂-Assisted Photocatalytic Process. *Appl. Catal. A* **2006**, *301*, 152–157.
- (59) Li, G. T.; Qu, J. H.; Zhang, X. W.; Liu, H. J.; Liu, H. N. Electrochemically Assisted Photocatalytic Degradation of Orange II: Influence of Initial pH values. *J. Mol. Catal. A: Chem.* **2006**, *259*, 238–244.
- (60) Song, S.; Hong, F. Y.; He, Z. Q.; Cai, Q. L.; Chen, J. M. AgIO₃-Modified AgI/TiO₂ Composites for Photocatalytic Degradation of *p*-Chlorophenol under Visible Light Irradiation. *J. Colloid Interface Sci.* **2012**, *378*, 159–166.
- (61) Martin, S. T.; Lee, A. T.; Hoffmann, M. R. Chemical Mechanism of Inorganic Oxidants in the TiO₂/UV Process: Increased Rates of Degradation of Chlorinated Hydrocarbons. *Environ. Sci. Technol.* **1995**, *29*, 2567–2573.
- (62) He, Z. Q.; Wang, C.; Wang, H. Y.; Hong, F. Y.; Xu, X. H.; Chen, J. M.; Song, S. Increasing the Catalytic Activities of Iodine Doped Titanium Dioxide by Modifying with Tin Dioxide for the Photodegradation of 2-Chlorophenol under Visible Light Irradiation. *J. Hazard. Mater.* **2011**, *189*, 595–602.
- (63) Chia, L. H.; Tang, X. M.; Weavers, L. K. Kinetics and Mechanism of Photoactivated Periodate Reaction with 4-Chlorophenol in Acidic Solution. *Environ. Sci. Technol.* **2004**, *38*, 6875–6880.
- (64) He, Z. Q.; Xie, L.; Tu, J. J.; Song, S.; Liu, W. P.; Liu, Z. W.; Fan, J. Q.; Liu, Q.; Chen, J. M. Visible Light-Induced Degradation of Phenol over Iodine-Doped Titanium Dioxide Modified with Platinum: Role of Platinum and the Reaction Mechanism. *J. Phys. Chem. C* **2010**, *114*, 526–532.
- (65) Thuan, D. B.; Kimura, A.; Ikeda, S.; Matsumura, M. Determination of Oxygen Sources for Oxidation of Benzene on TiO₂ Photocatalysts in Aqueous Solutions Containing Molecular Oxygen. *J. Am. Chem. Soc.* **2010**, *132*, 8453–8458.
- (66) Xiao, Z. G.; Bruck, M. A.; Enemark, J. H.; Young, C. G.; Wedd, A. G. A Catalytic Cycle Related to Molybdenum Enzymes Containing [Mo^{VI}O₂]²⁺ Oxidized Active Sites. *Inorg. Chem.* **1996**, *35*, 7508–7515.
- (67) Montoya, J. F.; Ivanova, I.; Dillert, R.; Bahnemann, D. W.; Salvador, P.; Peral, J. Catalytic Role of Surface Oxygens in TiO₂ Photooxidation Reactions: Aqueous Benzene Photooxidation with Ti¹⁸O₂ under Anaerobic Conditions. *J. Phys. Chem. Lett.* **2013**, *4*, 1415–1422.